Nuclear Engineering and Technology 59 (2027) 104678

Contents lists available at ScienceDirect

Nuclear Engineering and Technology

journal homepage: www.elsevier.com/locate/net

Original Article

Impact of correcting beam hardening and detector response function in photon-counting X-ray imaging when using anti-coincidence mode

Hiroaki Hayashi [a,*], Rina Nishigami [b], Daiki Kobayashi [b], Takuya Kasue [b], Natsumi Kimoto [c], Takashi Asahara [d]

[a] College of Transdisciplinary Sciences for Innovation, Kanazawa University, Kakuma-machi, Kanazawa, Ishikawa, 920-1192, Japan
[b] Graduate School of Medical Sciences, Kanazawa University, 5-11-80, Kodatsuno, Kanazawa, Ishikawa, 920-0942, Japan
[c] Department of Radiological Science, Faculty of Health Sciences, Junshin Gakuen University, 1-1-1 Chikushigaoka, Minami-Ku, Fukuoka, 815-8510, Japan
[d] Department of Radiological Technology, Faculty of Health Sciences, Okayama University, 2-5-1 Shikata-cho, Kita-Ku, Okayama, 700-8558, Japan

ARTICLE INFO

Keywords:
X-ray non-destructive testing
Photon-counting detector
Coincidence summing
CdTe detector
X-ray imaging

ABSTRACT

X-ray imaging using photon-counting detectors (PCDs) allows for the calculation of quantitative images such as the effective atomic number (Z_{eff}). However, physical phenomena such as characteristic X-ray emission and charge sharing can cause incomplete total absorption events during signal generation, which reduces the accuracy of X-ray penetration analysis. To solve the problem, an anti-coincidence mode (ACM) has been developed, but complete correction has not been established. We aimed to investigate the accuracy of Z_{eff} image when the proposed software-based corrections, namely beam hardening and response function corrections, are added to the hardware-based correction of the ACM. The response function was calculated using the Monte-Carlo simulation code. In a simulation study, we analyzed a phantom composed of virtual materials with Z_{eff} values of 4–16. While sufficient accuracy cannot be achieved by applying only the ACM, it was demonstrated that low-noise Z_{eff} images can be obtained by applying our correction. Furthermore, it was demonstrated that Z_{eff} images of food samples can be generated by using actual non-destructive testing equipment with a 10 m/min transportation speed. In conclusion, our correction procedure can maximize the performance of PCDs, and our findings are essential for promoting imaging techniques concerning quantitative images.

1. Introduction

Non-destructive imaging using polychromatic X-rays is an important diagnostic technique in medicine and industry [1]. The traditional method is to visualize the shadow image of the X-rays penetrating the objects. For achieving this objective, scintillation detectors (indirect conversion detectors) have been used, which is usually operated as an energy integrating detector (EID) [2]. However, this type of detector has limitations in terms of pixel size downsizing, and to obtain attenuation information for different energy X-rays requires measurements using multi-layered detectors or multiple exposures with different tube voltages [3,4].

In recent years, technological advancements in detectors have led to the practical application of imaging detectors using direct conversion semiconductor detectors [5]. Semiconductor detectors have been reported to enable downsizing of pixels and improve spatial resolution for imaging. Furthermore, owing to its high detection efficiency, attempts are being made to acquire images with low X-ray exposure (low exposure dose), which is very important for medical applications [6–9]. However, the advantages of using semiconductor detectors are not limited to them. Because semiconductor detectors operate as energy-resolving photon-counting detectors (PCDs) that can measure each individual X-ray photon and analyze its energy information [10–12], attenuation values of X-ray photons of different energies can be acquired even when a single irradiation of polychromatic X-rays is used.

By analyzing data on differential X-ray attenuation, it is possible to generate quantitative images that reflect the physical properties of the object. Photon-counting CT enables the generation of virtual monochromatic X-ray images (VMIs), which can perform image analysis using information by means of different X-ray energies. For example, algorithms for calculating effective atomic number (Z_{eff}) images [13,14] and effective physical density (ρ_{eff}) images [15–17] have been proposed. While the VMI used in clinical equipment consists of data that has

* Corresponding author.
E-mail addresses: hayashi.hiroaki@staff.kanazawa-u.ac.jp (H. Hayashi), nishigami.rina@gmail.com (R. Nishigami), kobayashi.daiki.2022@gmail.com (D. Kobayashi), takuya.kasue.1120@gmail.com (T. Kasue), natsumi.kimoto.0717@gmail.com (N. Kimoto), takashi.asahara.111@gmail.com (T. Asahara).

https://doi.org/10.1016/j.net.2026.104678
Received 29 April 2026; Received in revised form 20 August 2026; Accepted 24 August 2026
Available online 1 September 2026

Abbreviations:

PCD	Photon-counting detector
ACM	Anti-coincidence mode
Z_{eff}	Effective atomic number
$\mathbf{R}^{(1)}$	Response function that reflects radiation transportation and absorptions in the pixel of interest
$\mathbf{R}^{(2)}$	Response function that reflects charge collecting process (charge sharing effect)
FEP	Full energy peak
P	A parameter for peak efficiency in $\mathbf{R}^{(2)}$
R	A parameter for energy resolution in $\mathbf{R}^{(2)}$
SD	Standard deviation
CG	Course gain
C(i)	Counts value with course gain i

already undergone the various corrections discussed in this paper, commercially available PCD line sensors typically provide only raw count data, requiring the user to perform these corrections.

In order to analyze X-ray images with different energies based on physical theory and calculate novel quantitative images, it is necessary to correct imperfections in the obtained image data. As for PCDs, CdZnTe and CdTe are highly feasible as practical semiconductor materials. They have an Z_{eff} of approximately 50, and therefore, the characteristic X-rays generated during the radiation detection (absorption) process also have high energy (approximately 20-30 keV). Therefore, these detector materials are causing problems in which the response functions of the detector become complex [10,11]. Furthermore, a problem with multi-pixel detectors has been reported that there is the charge sharing effect, in which the charge generated within the detector pixel is dispersed to adjacent pixels when reading out the signals [18–20]. As a countermeasure against the charge sharing effect, a procedure has been proposed that uses hardware to add up the charges scattered in the surrounding pixels [21,22]. In the photon-counting line sensor used in this study (provided by Varex Imaging Corporation), this mode is called the “anti-coincidence mode (ACM)” and has been used in various imaging experiments [23,24].

It is known that data obtained via PCD does not perfectly reflect the true X-ray attenuation data, even when hardware-based corrections are applied. For example, Bushe et al. addressed the issue of zero counts in a computed tomography (CT) study [23]. In their study, by correcting zero-count data with statistical modelling, it was possible to align the CT values of low-dose and high-spatial-resolution PCD-CT images with those of standard-dose and standard-resolution PCD-CT images. Although the quantifiability of CT values has been investigated, there is no mention of generating quantitative images based on CT values. The statistical method proposed by Bushe et al. and the physical correction procedure presented in this study are complementary; therefore, combining them is expected to improve accuracy in ultra-low-dose imaging. Marupudi et al. have conducted research on Breast CT using PCDs, and reported on the effectiveness of using ACM [24]. Their research evaluates visibility, specifically in terms of improved spatial resolution and reduced image noise, but does not address quantitative material identification performance.

It has also been reported that the values measured with PCDs do not indicate the correct amount of X-ray attenuation by analyzing X-ray spectra. Ding et al. have reported that measured X-ray spectra differ from theoretically estimated X-ray spectra [25]. Therefore, they demonstrated that by formulating a semi-empirical correction equation, and they could recover spectral information that can improve material decomposition performance for three types of materials. While Ding et al. [25] developed an empirical, image-based polynomial calibration to mitigate spectral distortion in single-pixel PCDs, our approach adopts a physics-based framework specifically tailored for a PCD operating in ACM. Unlike their empirical count restoration, our study systematically quantifies the combined hardware-software contribution to high-precision Z_{eff} estimation for substance identification. Table 1 summarizes the differences between this study and previous studies.

The purpose of this study is to demonstrate that software correction is required for Varex Imaging sensors used in non-destructive testing, even when PCDs are operated in ACM. Fig. 1 shows a conceptual diagram of the study. The software processing corrects for the beam-hardening effect and for detector response functions. Although the basic calculation procedure of software processing was proposed by Kimoto et al. [26,27], their system was designed for single-pixel mode (SPM). In other words, the data used in their paper relates to SPM and cannot be directly applied to ACM. In this study, we newly calculated the response functions for ACM. If accurate attenuation data can be obtained as a result of the present study, it is expected that the accuracy of various quantitative images derived using PCDs [28,29] can also be improved.

Using Fig. 2, we will explain the reason why the detector response function must be considered in addition to ACM. Case **A** illustrates a scenario where the incident X-ray's total energy is fully absorbed within a single pixel; this ideal case yields undistorted energy signal. Case **B** depicts a situation where characteristic X-rays are generated during the absorption process. The energy signal distributes across neighboring pixels. Although the signal from the pixel of interest alone does not correspond to the total energy, the ACM allows these signals to be summed. Case **C** represents a scenario where characteristic X-rays escape the detector. Even when the ACM is used, we cannot identify the true energy value. Therefore, software-based correction is required. Similarly, events involving X-ray penetration shown in Case **D** cannot be corrected without employing software-based correction.

2. Materials and methods

2.1. Z_{eff} image generation procedure

This section describes an algorithm for calculating effective atomic number images that can be calculated using a non-destructive X-ray imaging system equipped with a PCD, and explains the importance of considering the response function in constructing the algorithm.

Fig. 3 shows a schematic of the algorithm used to analyze experimentally obtained image data and calculate the Z_{eff} value of the object. The photon counting system used in this paper is capable of simultaneously acquiring image data of low-energy bin (30–40 keV) and high-energy bin (40–60 keV), and polychromatic X-rays with a tube voltage of 60 kV were used. The measured data represents the count value of X-rays penetrating the object for each energy bin. The attenuation factor (μt) of X-rays, in which μ indicates linear attenuation factor [30] and t is thickness, is calculated using the Lambert-Beer law:

$$\mu t = \ln\left(\frac{I_0}{I}\right), \tag{1}$$

where I_0 and I are the number of X-ray photons incident on the object and the number of X-ray photons penetrating the object, respectively.

By obtaining the X-ray attenuation factors for both the low-energy (μt_{low}) and high-energy (μt_{high}) bins, and calculating the ratio of them, we can derive a physical quantity that correlates with Z_{eff}. Using a theoretical calculation database [30], a reference curve $f(\mu t_{high}/\mu t_{low})$ that can be derived from a correlation relationship between the $(\mu/\rho)_{high}/(\mu/\rho)_{low}$ ratio and atomic number Z was generated in advance. Then, Z_{eff} can be determined by the following equation [26]:

$$Z_{eff} = f\left(\frac{\mu t_{high}}{\mu t_{low}}\right). \tag{2}$$

It should be noted that equations (1)&(2) are valid only for

Table 1
Differences between this study and previous studies.

Authors	Purpose	Procedure	PCD	Subject of evaluation
Bushe et al. (2023) [23]	Correction of statistical bias in logarithmic calculations caused by data deficiency (zero counts) at low dose levels	Mathematical estimation	Single-pixel mode	HU(Hounsfield unit) value bias, image noise (SD/NPS), spatial resolution (MTF)
Ding et al. (2012) [25]	Image-based correction via polynomial fitting to measured data	Empirical procedure	Single-pixel mode	Count value and attenuation factor (μ)
Present study	Accurate substance identification via quantitative Z_{eff} imaging	Correction modeling of detector response functions and beam hardening based on physical mechanisms	Anti-coincidence mode	Quantitative accuracy of effective atomic number (Z_{eff})

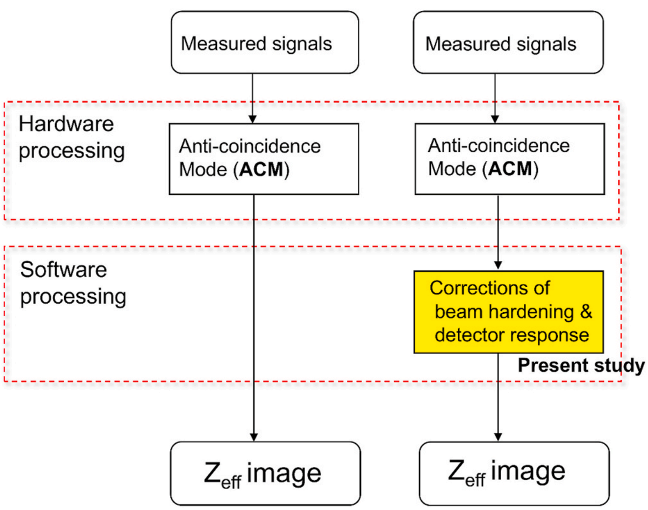

Fig. 1. The concept of this study. In addition to a hardware-based anti-coincidence mode, we propose a software-based correction procedure.

monochromatic X-rays, and therefore, in order to perform the analysis of the measured data, the correction shown on the right side of Fig. 3 must be applied. The first correction element is the beam hardening correction, which corrects for the change in effective energy caused by the hardening of X-ray quality when penetrating the object. The second

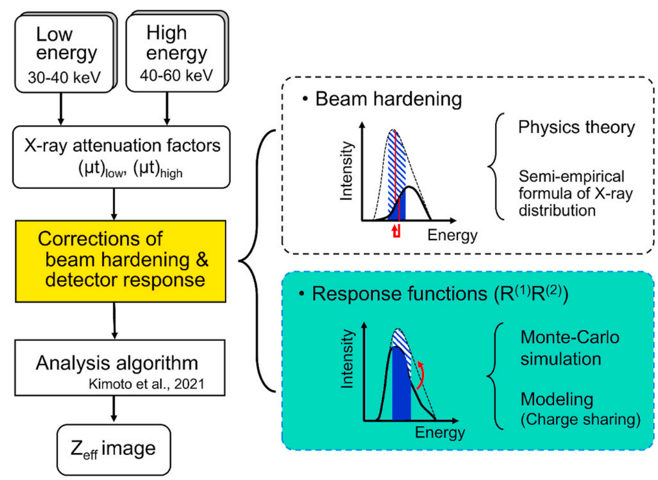

Fig. 3. The relationship between the effective atomic number calculation algorithm and corrections for beam hardening & detector response.

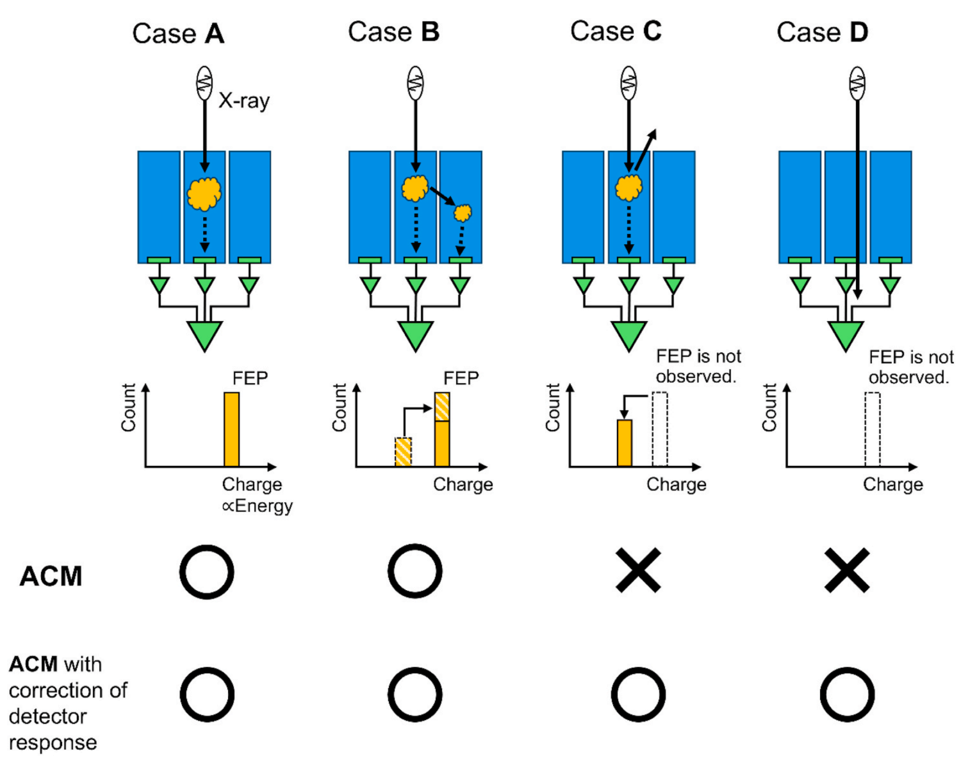

Fig. 2. Diagram explaining the reason why corrections for detector response functions must be performed in addition to ACM.

correction element is related to the response functions of the detector. In practice, both of the above effects can be corrected simultaneously with a single correction calculation [26]. The specific procedure for creating the correction curve is summarized in the Appendix.

2.2. Calculation of response function

Response functions were calculated by Electron Gamma Shower ver. 5 (EGS5) [31]. The EGS5 code is a computational code particularly well-suited for low-energy photon transport calculations and has been used in shielding calculations etc. [32]. Table 2 compares the conditions for calculating response functions. The response functions of ACM were newly calculated in this study.

Upper panel in Fig. 4 shows the arrangement used for the simulation. The detector part consists of cadmium telluride ($\rho = 5.85$ g/cm^3) with a thickness of 0.75 mm [33]. The detector's planar size was set to be 10 mm $\times$ 10 mm. A summing up calculation is mimicked when the energy information is divided into the surrounding pixels. Since this process is performed on 2 $\times$ 2 pixels, in calculating the response function, the detector size was virtually set to 200 μm $\times$ 200 μm, and the central 100 μm $\times$ 100 μm area was set as the irradiation field. In the calculations, the generation of characteristic X-rays caused by the photoelectric effect were precisely reproduced. The intense K X-rays of Cd are 23 keV and 26 keV, and those of Te are 27 keV and 31 keV [34,35].

The bottom panel of Fig. 4 shows a conceptual diagram of the ACM. In this mode, the distribution of charge among four adjacent pixels is assumed. In the illustrated example, the charge is split into portions of 75%, 10%, 10%, and 5%. The ACM algorithm identifies the "winner" pixel and assigns the total summed energy to that pixel. The ACM is designed to correct for charge spreading within a cluster of 2$\times$2 pixels.

The response function was calculated by irradiating 10^7 X-ray photons into the pixel of interest. The energy of incident X-rays was varied from 0.2 keV to 140 keV, in increments of 0.2 keV. The parallel calculations were performed using a workstation (Ryzen Threadripper pro, 5995WX, 64 cores, 2.70 GHz), and the typical time taken for the calculations was 0.2 days.

2.3. Simulation of virtual X-ray image

By performing simulations study, we quantified the usefulness of ACM and the impact of correcting for the effects of beam hardening and

Table 2
Comparison of differences in response functions between this study and previous studies.

	Previous studies	Present study
Reference	[26,27]	-
Operating mode	Single pixel mode (SPM)	Anti-coincidence mode (ACM)
Detector material	CdZnTe ($\rho = 5.8$ g/cm^3)	CdTe ($\rho = 5.85$ g/cm^3)
Detector thickness	1.5 mm	0.75 mm
Pixel size	200 μm $\times$ 200 μm	100 μm $\times$ 100 μm (The obtained image is binned using software processing to make it 200 μm $\times$ 200 μm)
Response function calculation	EGS5	EGS5
Charge sharing modeling	Full energy peak and step function	No need to take into consideration
Energy threshold	Low energy (20-32 keV) Middle energy (32-40 keV) High energy (40 -50 keV)	Low energy (30-40 keV) High energy (40-60 keV)
Tube voltage	50 kV	60 kV

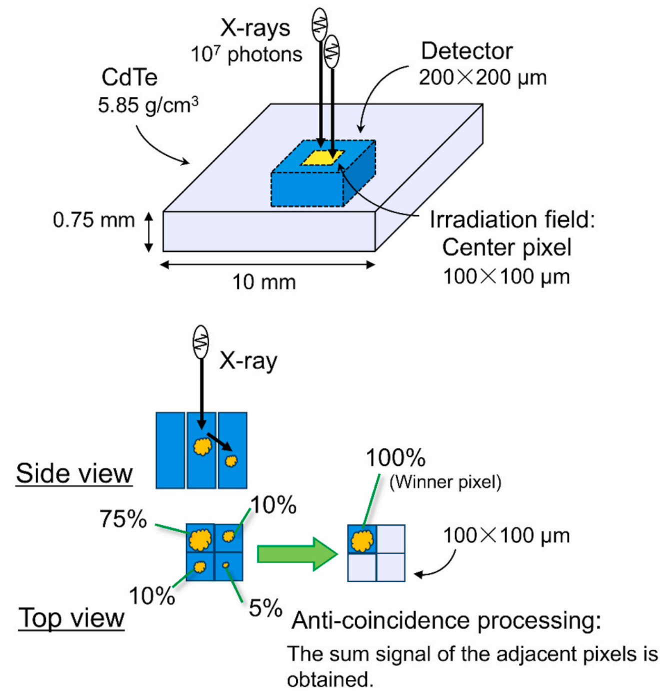

Fig. 4. Monte-Carlo calculation system for radiation transport calculations in detectors. The response function of the ACM was reproduced using the Monte Carlo simulation code EGS5. The upper figure shows the simulation geometry, and the lower figure is a conceptual diagram of the ACM.

response functions when calculating Z_{eff} images.

The X-ray image simulations were performed using the simulator developed by our research group [36], in which response functions calculated newly in this study were incorporated. The simulator is an in-house program written in Mathematica programming software (Wolfram Research, Inc., U.S.A.) that can calculate X-ray projection images based on the phantom design. This simulator can calculate the effects of X-ray attenuation in the object and the response function of the detector using the Monte-Carlo method. Image noise associated with Poisson statistics was taken into consideration, and other noise sources, such as electrical noise, were ignored.

In this study, we evaluated the image quality of a simple virtual phantom. The phantom's cross-section shape is 100 $\times$ 100 pixels (10 $\times$ 10 mm^2). The atomic number Z values for these materials were set to 4, 7, 10, 13, and 16. The phantom thickness (mass thickness: ρt) was assumed to be 0.1, 0.2, 0.5, 1, 2, 5, 10, 20, and 50 g/cm^2 in terms of mass thickness. The dose conditions were adjusted so that the surface dose was 0.07 mGy, which was 5.7 times smaller than that used in general medical X-ray examinations [37]. The obtained images (count images of 30–40 keV and 40–60 keV) were converted into Z_{eff} images using the Z_{eff} calculation algorithm, and the mean and standard deviation of each measurement region set as a phantom were calculated.

2.4. Experiments using non-destructive testing equipment

In this study, two types of experiments were conducted. The first experiment was to estimate the parameters of the detector, in which the X-ray spectrum without an object was measured with an image detector. The second experiment was an imaging experiment, aimed at demonstrating the Z_{eff} image.

The folded spectrum, taking into account the effect of the response function, was calculated as follows. The energy distribution of the X-ray spectrum emitted from the X-ray target was calculated using a semi-experimental formula under conditions of a tube voltage of 60 kV and total filtration of 2.4 mm aluminum [38]. The predicted theoretical

X-ray spectrum was folded by the response function $\mathbf{R}^{(1,2)} = \mathbf{R}^{(1)}\mathbf{R}^{(2)}$, and the folded spectrum was compared with the experimental data. The detector's response function is composed of elements $\mathbf{R}^{(1)}$ related to the calculation of radiation transport within the detector and elements $\mathbf{R}^{(2)}$ related to charge sharing. Various parameter combinations for P (Peak efficiency) and R (Resolution) were examined, and a parameter set was adopted that yielded the highest reproducibility. The parameter search range was $10\% \leq P \leq 100\%$ with increments of 5% and $20\% \leq R \leq 50\%$ with increments of 5%. In this study, a common parameter set was applied to all pixels.

X-ray spectra were measured using an in-line-type non-destructive testing system. Fig. 5 shows a schematic diagram of the experiment. The distance between the X-ray focal spot and the detector surface was 514.6 mm, and the line sensor (TDI350.1.60.075.N, Varex Imaging Corporation, U.S.A.) [23,24] was positioned in a direction that does not affect the X-ray heel effect [39]. The line sensor consisting of 14 sensor units has dimensions of 3584 × 60 pixels, in which the size of one pixel is 100 μm × 100 μm. The sensor is a CdTe-CMOS ($\rho = 5.85$ g/cm^3) with a sensor thickness of 0.75 mm. To reduce the data size of the obtained images, binning was performed on 2 × 2 pixels, and an image data (frame data) of 1792 × 30 pixels was taken, in which the central sensor unit with 128 × 30 pixels (=3840 pixels) was analyzed. This sensor allows setting only two different threshold energies at once. Then, signals related to threshold values (the course gain (CG) variable (i = 0 to 63)) were recorded. To measure the differential energy spectrum of polychromatic X-rays as shown in Fig. 5 (b-1), two images were acquired under values of i and i+1, and the difference in the count values of these images (C(i + 1) − C(i)) was calculated. This value was averaged over 3840 pixels, and the average of the difference value $\overline{\mathrm{C(i+1)}} - \overline{\mathrm{C(i)}}$ was measured. This procedure was performed for all CG settings to obtain X-ray spectrum. The energy calibration of the CG was performed using the endpoints of the X-ray spectra of 30 kV to 60 kV.

The experiments using X-ray images were performed as shown in Fig. 5 (b-2). Tube voltage and tube current were set as 60 kV and 2 mA, respectively. X-ray exposure time per 1 cm^2 surface was approximately 1 s. The objects were placed on a conveyor belt and transported at a speed of 10 m/min. Under this condition, the radiation dose at the surface of the conveyor belt was 0.07 mGy. This dose corresponds to measurement conditions under which the pile-up effect [40] is negligibly small. The energy bin settings were 30–40 keV for low-energy images and 40–60 keV for high-energy images. Namely, the image data required for a single Z_{eff} analysis consists of four images: low-energy and high-energy images, under conditions with and without samples. Using our algorithm, Z_{eff} images were analyzed, in which the reconstructed image size was 1792 × 1792 pixels.

To validate the methodology with the proposed correction, measurements were performed on phantoms made of polymethylmethacrylate (PMMA, $Z_{eff} = 6.5$) and aluminum ($Z = 13.0$), which have known Z_{eff} values. The phantom thicknesses were 1, 3, and 5 cm for PMMA, and 1, 1.5, and 2 cm for aluminum. The phantoms have a stepped structure, with each step having an area of 5 × 5 cm^2. Furthermore, a demonstration was conducted using actual food items with complex structures as targets. Spareribs containing both soft tissue ($Z_{eff} \approx 6.5$) and bone ($Z_{eff} \approx 13.0$) were selected as samples. For the PMMA and Al samples, Z_{eff} images were calculated, and the accuracy of these quantitative images was evaluated. On the other hand, since the true Z_{eff} values for the sparerib samples were unknown, the change in Z_{eff} values resulting from the application of correction was quantified.

3. Results and discussions

3.1. Calculation of response function

Fig. 6 shows the calculation results of the response function when applying ACM. The graphs on the left and right show $\mathbf{R}^{(1)}$ and $\mathbf{R}^{(2)}$ for incident X-rays at 80 keV, respectively. In $\mathbf{R}^{(1)}$, a full-energy peak (FEP)

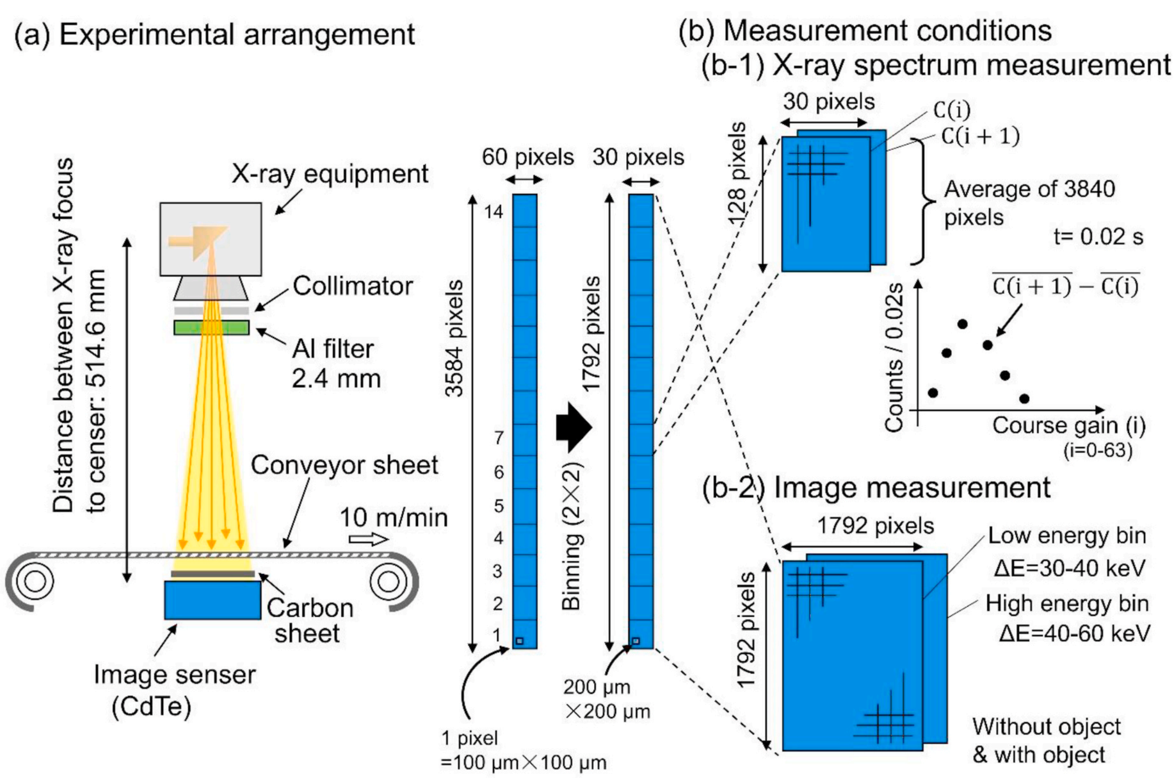

Fig. 5. (a) Experimental arrangement and (b) measurement conditions. To evaluate the detector response functions, the X-ray spectrum was measured under the condition without an object (b-1). In the image acquisition experiment, low-energy (30–40 keV) and high-energy (40–60 keV) images were measured under conditions with and without objects (b-2).

was observed at 80 keV, and intense characteristic X-ray escape peaks were also observed. Although components other than FEP are effectively suppressed by applying the ACM, escape peaks are clearly observed. This is because there are characteristic X-rays emitted towards the detector's surface direction (see Case **C** in Fig. 2). In $\mathbf{R}^{(2)}$, only the effect of energy resolution was taken into consideration. The graph on the bottom shows the fraction of each component of the response function. The actual proportion of FEP of 50 keV was approximately 67%, while scattered X-rays accounted for 31%. It is noteworthy that while ACM dramatically increases the proportion of FEP, nearly 30% of the components are related to scattered X-rays and escapes. This suggests that, since the FEP is not 100%, it is necessary to take into consideration the effect of the response function when quantitatively analyzing X-ray attenuation.

3.2. Folded X-ray spectrum

Fig. 7 shows a comparison between the measured X-ray spectrum and the estimated spectrum. The spectrum shown by the dashed line is the incident X-ray spectrum at a tube voltage of 60 kV. The red open circles represent measured data, while the blue lines represent the result of matching the incident X-ray spectrum folded with the response function. The X-ray spectrum obtained from the simulation shows good agreement with the experiments within the 30 keV to 60 keV range that is actually used for analysis. This indicates that the response function model we assumed in Fig. 4 accurately reproduces the actual physical phenomena.

The measured X-ray spectrum looks like a similar distribution to the incident X-ray spectrum. This is due to the high proportion of FEP in this system. However, the difference between them, which is indicated by the shaded area, is not negligible; specifically, it amounts to approximately 30%. The physical quantity we want to analyze is the information regarding X-ray attenuation in the object that is essentially included in the incident X-ray spectrum. As shown in Fig. 7, the measured spectrum differs from the incident X-ray spectrum; therefore, correction is required.

In actual PCD analysis, the pixel value in the X-ray image is determined by the integrated count value within an energy bin, which is indicated by the blue or red regions in the spectrum. This means that the X-ray spectrum shown in Fig. 7 cannot be directly analyzed; instead, corrections must be performed using only the count values from the low-energy and high-energy bins. This correction can be performed using the algorithm presented in Fig. 3.

3.3. Simulated image

Fig. 8 shows the results of Z_{eff} images of materials with Z_{eff} values ranging from 4 to 16. These results were obtained through simulation. In order to only evaluate the effects of beam hardening and the detector response function separated from the other error components, we conducted a simulation that excluded statistical uncertainty. Panel (1) shows the analysis results obtained with correcting for beam hardening and the response function; exact results were obtained for materials of all Z_{eff} materials. The procedure proposed in this paper derives a

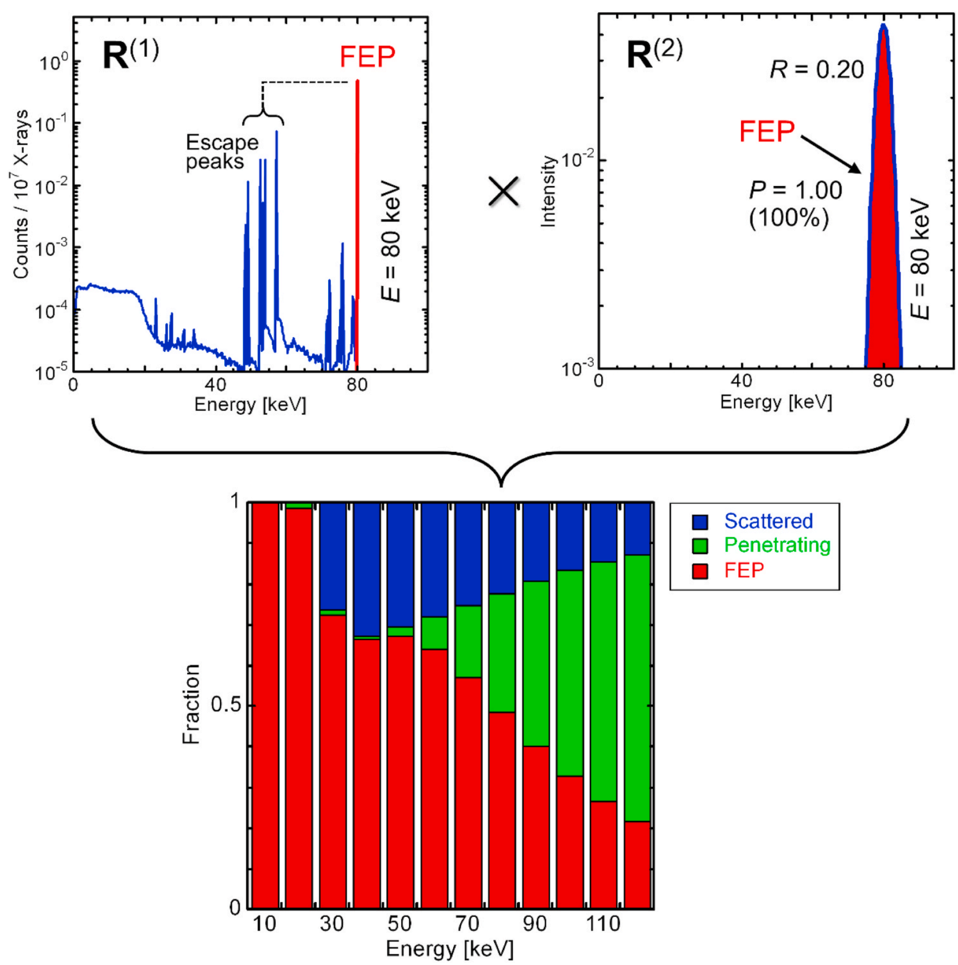

Fig. 6. Calculated response functions of CdTe detector when applying ACM. $\mathbf{R}^{(1)}$ is the result of spectrum calculated by Monte-Carlo simulation, and $\mathbf{R}^{(2)}$ is a model of charge sharing. Even when ACM is applied, the full-energy peak (FEP) component does not account for 100% of the total; therefore, these results indicate the necessity of taking into consideration the influence of the response function during attenuation analysis of X-rays.

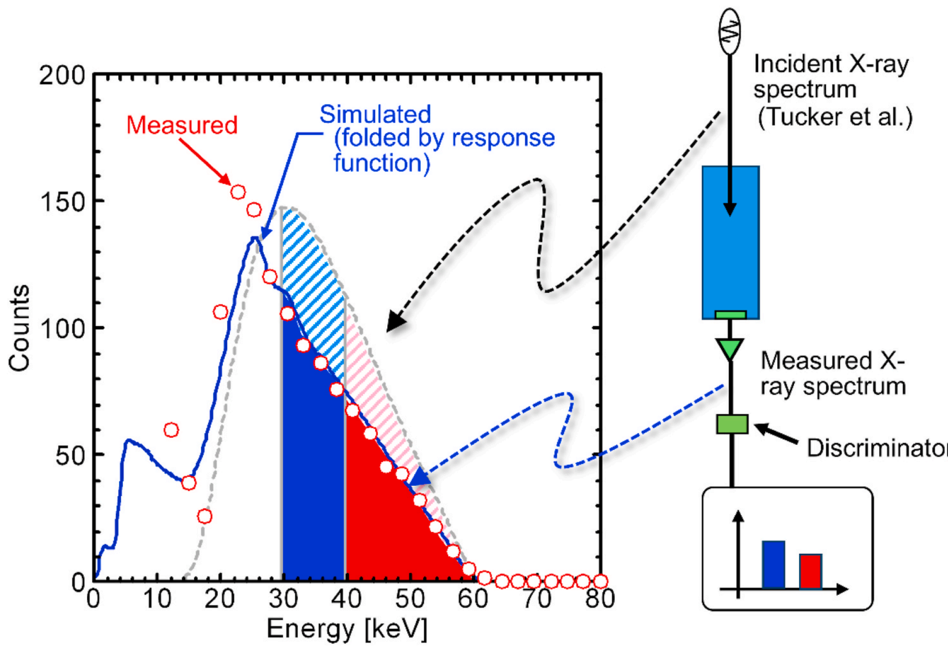

Fig. 7. Comparison of convolved X-ray spectra with experimentally measured one. We examined the shape of the X-ray spectrum and used it to estimate parameters related to the detector's response function, and also confirmed that no significant pile-up effect was observed.

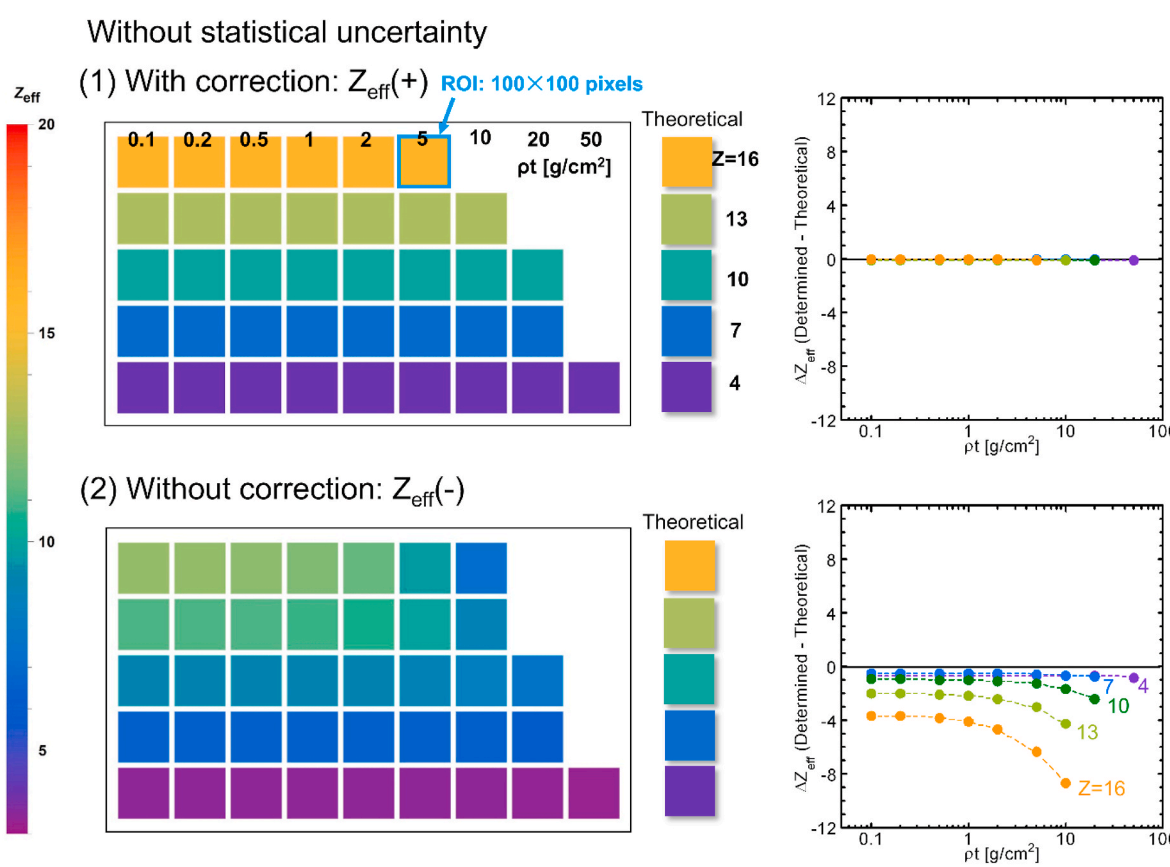

Fig. 8. Analysis results of Z_{eff} images for materials with Z_{eff} values ranging from 4 to 16, which were generated by simulation. These results were calculated by eliminating the effects of statistical fluctuations. Panel (1) shows the analysis results for image data corrected for beam hardening and detector response using the proposed procedure, while panel (2) shows the analysis results for image data without the proposed corrections.

physically correct solution by mimicking the physical phenomena occurring within the object and detector. Consequently, the residuals (ΔZ_{eff} = determined Z_{eff} - theoretical Z_{eff}) become zero as shown by the right figure. Materials with high Z_{eff} and high ρt could not be analyzed, because their measurement values are less than 1 count because of high attenuation of X-rays. In contrast, as shown in panel (2), when corrections for beam hardening and the response function were not applied, the obtained Z_{eff} values exhibited a systematic difference as Z_{eff} increased. This indicates that data failing to account for beam hardening and the detector response function contain inherent sources of systematic uncertainty, making it impossible to calculate the correct solution. For materials with $Z_{eff} = 4$ and 7, the systematic uncertainty is relatively small; ΔZ_{eff} values remain below 1. However, when Z_{eff} exceeds 13, ΔZ_{eff} rises above 2, which cannot be acceptable.

Fig. 9 shows the results of calculations with the addition of statistical noise corresponding to a dose of 0.07 mGy, in which the same objects as presented in Fig. 8 were revaluated. Fundamentally, the results followed a similar trend to those in Fig. 8, demonstrating that accurate Z_{eff} values can be obtained by correcting for beam hardening and the detector response function. In the Z_{eff} image, the pixels shown in white are error pixels; they correspond to pixels for which the Z_{eff} calculation algorithm failed to yield a valid solution. The inclusion of statistical noise resulted in a failure to calculate the correct Z_{eff} when objects have insufficient X-ray attenuation. This trend was particularly pronounced for objects with low Z_{eff} and low ρt. As shown in the figure on the right, the variation in Z_{eff} values (δ: fluctuation range of the median of Z_{eff} value) was minimized at $\rho t = 2$ g/cm^2. Therefore, the range of Z_{eff} value fluctuation ($\delta_{\rho t = 2}$) was examined. The $\delta_{\rho t = 2}$ was 2.33 for "(1) with correction", whereas it was 5.96 for "(2) without correction". It was demonstrated that applying the correction proposed in this paper can reduce the fluctuation in Z_{eff} calculations to less than half.

Fig. 10 presents the results of a re-analysis of the data in Figs. 8 and 9 with a clearer format; regions where $\Delta Z_{eff} \leq 1$ are indicated by solid squares. The upper panel shows the image analysis results obtained without considering statistical uncertainty, which clearly demonstrated the effect of systematic uncertainties can be removed by applying our correction procedure. The lower panel shows the results obtained when statistical uncertainties were considered, which reflects both the uncertainty component and statistical uncertainty component in the designed X-ray system. Result (1) was obtained by applying the proposed correction procedure. Compared to result (2) that was obtained without applying the correction procedure, the $\Delta Z_{eff} \leq 1$ range is drastically expanded. This is particularly evident for $Z_{eff} = 13$. In biological sample analysis including non-destructive food inspection, soft tissue has an Z_{eff} of approximately 7, while bone is around 13 [28]. This means that by applying the proposed correction procedure, it is possible to accurately analyze objects that include not only soft tissue but also bone.

The subject of this paper is to quantitatively demonstrate that non-negligible changes in Z_{eff} values occur when corrections for beam hardening and detector response functions are applied. Table 3 presents numerical data showing the impact of these corrections on all samples with $Z_{eff} = 7$ and $Z_{eff} = 13$, based on data generated through simulation (see Fig. 9). The Wilcoxon rank test was performed on all data, and all results showed a significant difference, with a p-value of 0.01 or less.

3.4. Measured images

Fig. 11 shows the evaluation results of the Z_{eff} images for PMMA and Al. The top-left panel of Fig. 11 shows a photograph of the phantoms, and the bottom-left panel shows the corresponding Z_{eff} image. The Z_{eff} image has been cropped to make the subject appear larger. As shown on the right, with the exception of the 1 cm thick PMMA sample, the results showed good agreement within a range of ±0.5 in Z_{eff} values, which is a similar level of accuracy with that of previous ERPCD studies [26]. For the 1 cm thick PMMA sample, however, statistical uncertainties were significant, and numerous "error pixels" appeared as white spots in the

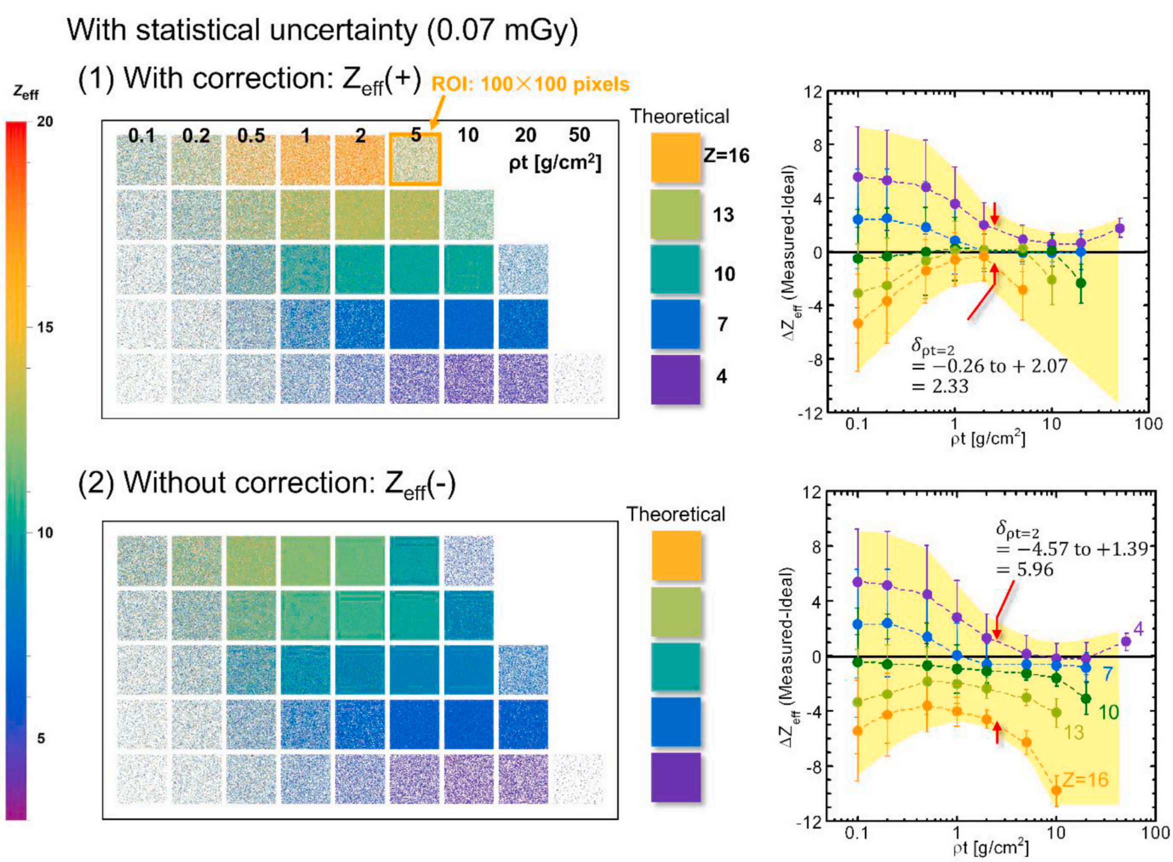

Fig. 9. Z_{eff} image calculation results of analyzing simulated images of materials with Z_{eff} values ranging from 4 to 16, in which statistical fluctuations equivalent to 0.07 mGy were taken into consideration. Panel (1) shows the results obtained using the proposed correction procedure, while panel (2) shows the results without the correction.

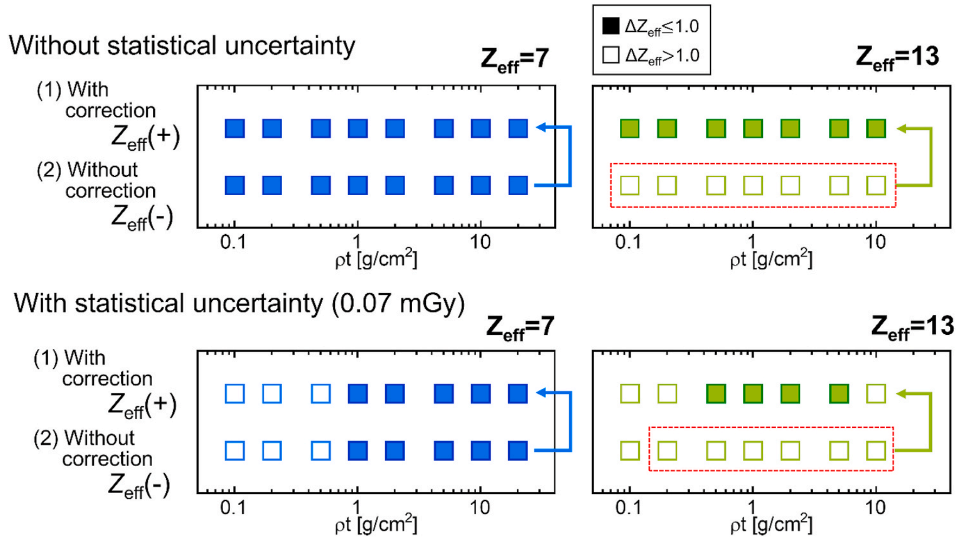

Fig. 10. Re-analysis results of the data shown in Figs. 8 and 9. The range where ΔZ_{eff} is less than 1.0 is indicated for (1) with correction and (2) without correction. The top panel shows the analysis results for simulated images with statistical uncertainties removed, while the bottom panel shows those including statistical uncertainties.

Table 3
Quantitative analysis results for the Z_{eff} image generated by simulation with statistical uncertainties (see Fig. 9). It was shown that the Z_{eff} values vary depending on applying the proposed correction procedure.

Object	ρt [g/cm^2]	Z_{eff}		
		With correction $Z_{eff}(+)$	Without correction $Z_{eff}(-)$	Difference[a] $Z_{eff}(-)$ - $Z_{eff}(+)$
$Z_{eff} = 7$	0.1	9.48 ± 3.72	9.40 ± 3.97	−0.08
	0.2	9.51 ± 3.72	9.45 ± 3.88	−0.06
	0.5	8.90 ± 2.15	8.45 ± 3.41	−0.45
	1	7.86 ± 2.52[b]	7.13 ± 2.32[b]	−0.73
	2	7.05 ± 1.54[b]	6.45 ± 1.50[b]	−0.60
	5	6.97 ± 0.85[b]	6.42 ± 0.79[b]	−0.55
	10	6.97 ± 0.72[b]	6.36 ± 0.64[b]	−0.61
	20	7.04 ± 1.33[b]	6.17 ± 1.08[b]	−0.87
$Z_{eff} = 13$	0.1	9.93 ± 3.70	9.74 ± 3.77	−0.19
	0.2	10.52 ± 3.54	10.28 ± 3.55	−0.24
	0.5	12.38 ± 2.85[b]	11.22 ± 2.47	−1.16
	1	13.12 ± 2.20[b]	11.02 ± 1.37	−2.10
	2	13.23 ± 1.62[b]	10.71 ± 0.75	−2.52
	5	13.26 ± 1.70[b]	10.03 ± 0.58	−3.23
	10	10.95 ± 1.81	8.92 ± 1.02	−2.03

[a] This is the difference between the mean values of Z_{eff} calculated with and without corrections of beam hardening and detector response.
[b] The difference from the correct value is within $\Delta Z_{eff} \leq 1$.

Z_{eff} image; this suggests a possibility of insufficient radiation doses. The fact that the validation results for the Z_{eff} images demonstrated good agreement indicates the robustness of the analysis procedure developed in this study.

Fig. 12 shows an Z_{eff} image of spareribs, which was measured with actual non-destructive food inspection system. Although these Z_{eff} images were acquired at a transport speed of 10 m/min, no significant image noise that would hinder analysis was observed, and sufficient-quality images were obtained. Result (1) shows the Z_{eff} image obtained using our proposed correction, while result (2) shows that without correction. The figure at the bottom right displays the difference image between them. It was found that the difference image reveals a significant discrepancy of −1 to −2 in areas containing bone and soft-tissue, and a difference of 0 to −1 in areas only containing soft-tissue. These results are consistent with the simulation results presented in Table 3. In other words, both simulations and actual measurements have confirmed the scientific conclusion that an additional software-based correction should be applied even when using the ACM.

A limitation of this study is that the trade-off between spatial resolution and material identification accuracy was not investigated. Although 2×2 binning was initially applied to the experimental data to improve computational speed and reduce statistical fluctuations, this is considered to have degraded the spatial resolution. Future work must integrate an analysis of spatial resolution to optimize the system.

3.5. *Impact of the present study*

The academic significance of this study lies in demonstrating that it is necessary to correct for beam hardening and the response functions of the detector even when quantitatively analyzing X-ray attenuation using a photon-counting type image detector equipped with an ACM. In research on photon-counting-type detection technologies using semiconductor detectors, basic research has been actively conducted on the importance of charge sharing correction and development of ACM [18–20]. However, when characteristic X-rays escape towards the surface of the detector, existing hardware-based correction methods cannot detect these characteristic X-rays as indicated by Fig. 2. Therefore, we developed a procedure to correct these effects using software-based correction, and showed that this effect significantly contributes to the quantitative analysis of X-ray attenuations.

Fig. 12 demonstrates the practical applicability of our procedure for analyzing measured X-ray images. This study demonstrated that, using data acquired in ACM with a transport speed of 10 m/min (commonly used in non-destructive tests), the proposed algorithm could correct beam hardening and the detector's response function, resulting in Z_{eff} images with analyzable quality. The limitations of this study are as follows. The image settings used in this paper have not yet been optimized, and it is thought that higher quality images can be generated with higher tube voltage measurements [36]. In this study, we investigated the experiment, where pulse pile-up does not occur. A key challenge for obtaining higher-quality X-ray images in the future is to successfully perform measurements at high dose rates. Recently, our research group proposed a pulse pile-up correction method for SPM measurement systems [40] and developed a methodology to correct data acquired in the high-dose range. As the next step, we want to establish a robust methodology that incorporates pulse pile-up correction for ACM.

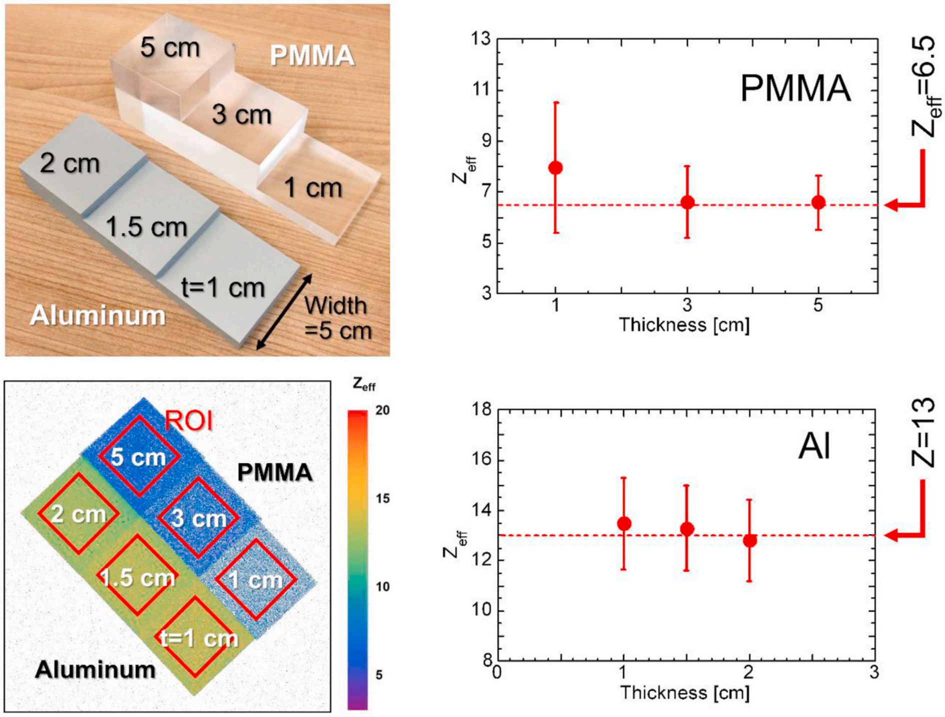

Fig. 11. Results of verification experiments using phantoms which have known atomic numbers. Measurements were performed on PMMA phantoms with thicknesses of 1–5 cm and aluminum phantoms with thicknesses of 1–2 cm. The Z_{eff} values obtained in the experiment agreed well with the theoretical values, in which the correction procedure proposed in this study were applied.

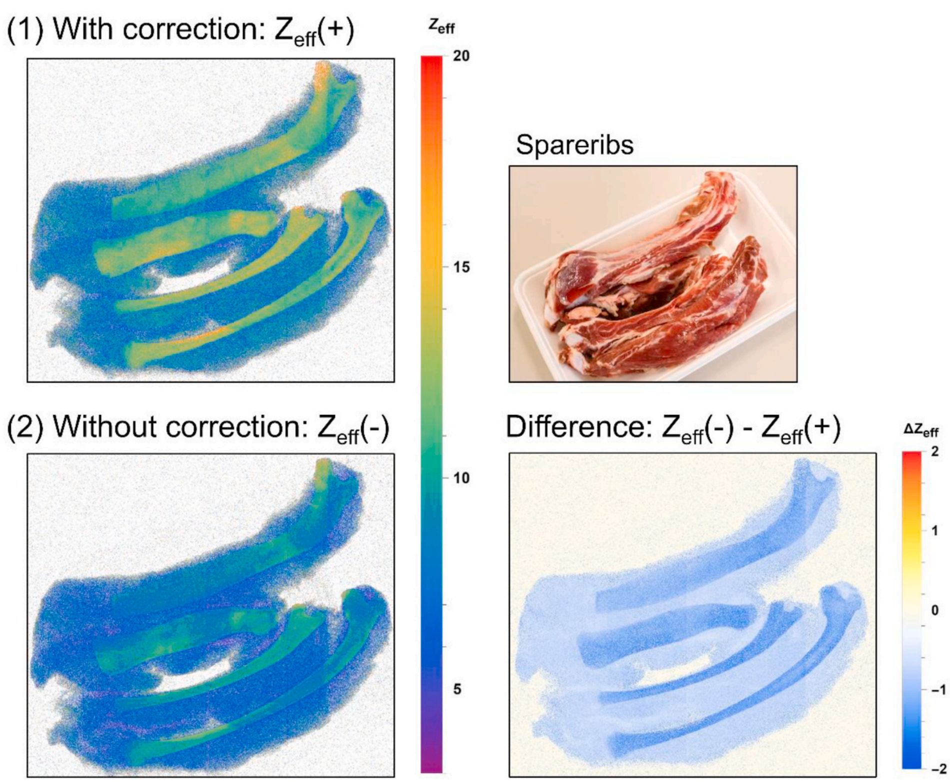

Fig. 12. Z_{eff} image of spareribs that was experimentally measured with ACM. Images without correction show systematically lower Z_{eff} values compared to those with correction.

4. Conclusion

We conducted imaging research using a CdTe photon-counting image detector based on polychromatic X-ray exposure and analyzed image quality focusing on the reproducibility of Z_{eff}. The simulation image using virtual phantoms with $4 \leq Z_{eff} \leq 16$ and $0.1 \leq \rho t \leq 50$ g/

cm^2, and experimental image of food samples transported at a speed of 10 m/min were analyzed. Even in anti-coincidence mode (ACM), software correction reduces the systematic uncertainty of Z_{eff} calculation by approximately 61% (from $\delta_{\rho t = 2} = 5.96$ to 2.33). Our study demonstrated that applying corrections for the effects of beam hardening and the detector response function is highly impactful, even when X-rays are measured with an ACM.

In summary, while existing approaches rely on post-reconstruction statistical estimation (e.g., Bushe et al. [23]) or empirical polynomial fitting (e.g., Ding et al. [25]) in conventional single-pixel PCDs, our proposed framework combines hardware-based ACM with physics-based model corrections. This hybrid hardware-software strategy effectively resolves residual spectral distortions and establishes a robust, highly accurate foundation for quantitative Z_{eff} estimation and substance identification.

CRediT authorship contribution statement

Hiroaki Hayashi: Writing – original draft, Project administration, Methodology, Investigation, Conceptualization. **Rina Nishigami:** Writing – review & editing, Methodology, Investigation, Formal analysis. **Daiki Kobayashi:** Software, Investigation. **Takuya Kasue:** Writing – review & editing. **Natsumi Kimoto:** Writing – review & editing, Visualization, Investigation. **Takashi Asahara:** Writing – review & editing, Visualization, Investigation.

Funding sources

This study was supported by Grants-in-Aid for Scientific Research [KAKENHI: 24K03306(Hayashi), 25K21586(Asahara), 25K21600 (Kimoto), 25KJ1355(Kobayashi)]. This work was also supported by the Sasakawa Scientific Research Grant from the Japan Science Society (Grant Number: 2026-6001).

Declaration of competing interest

The authors declare the following financial interests/personal relationships which may be considered as potential competing interests: The authors declare the following financial interests/personal relationships which may be considered as potential competing interests: This work was supported by JSPS KAKENHI Grant Number [KAKENHI: 24K03306 (Hayashi), 25K21586 (Asahara), 25K21600 (Kimoto), 25KJ1355 (Kobayashi)], and the Sasakawa Scientific Research Grant. Additionally, System Square Inc. Provided the experimental apparatus used in this study on a loan basis. The funders and the equipment provider had no role in the study design, data collection, analysis, decision to publish, or preparation of the manuscript.

Acknowledgement

This paper was supported by funding reported in the funding source section.

Appendix

This chapter provides supplementary explanations regarding a procedure for correcting effects of beam hardening and the response function of the detector.

Figure A1 shows a conceptual diagram of the correction curve. This correction is used to convert the X-ray attenuation (μt) obtained with polychromatic X-rays to that obtained with monochromatic X-ray. The horizontal axis represents mass thickness (ρt [g/cm^2]), and the vertical axis represents the X-ray attenuation coefficient (μt). As penetrating thicker objects, X-rays are more strongly affected by beam hardening and detector response. This results in a phenomenon in which the actually calculated μt value differs from the μt value estimated from the monochromatic X-ray. Therefore, the differences are simulated in advance for various thicknesses, and the measured μt is converted to an ideal μt by correcting it along the path indicated by the arrow in the left diagram of Fig. A1. At this time, to simplify the calculation process, the horizontal axis of the correction curve is multiplied by μ/ρ. By this way, the correct value always exists on the Y = X line. The correction curve is generally known as the beam hardening correction function, but it can be used to correct not only the beam hardening effect but also the response function of the detector simultaneously. Detailed explanations can also be found in our previous paper [26,27].

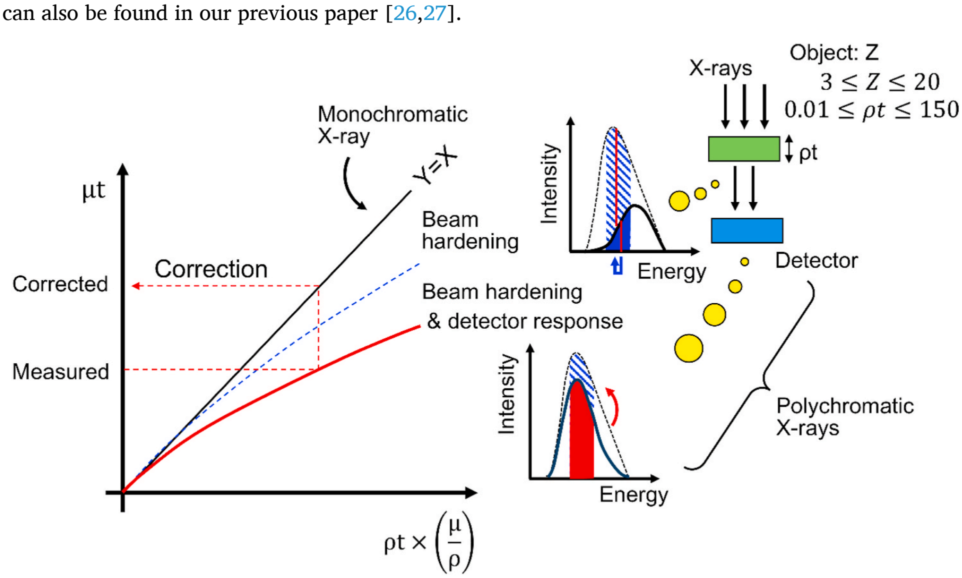

Fig. A1. Schematic diagram of correction curves for correcting beam hardening and detector response. This correction is used to convert the measured μt value based on polychromatic X-rays into those obtained using monochromatic X-ray. It should be noted that the correction curve varies depending on the atomic number (Z) of the object material, energy bin settings, tube voltage setting, and whether ACM was applied.

The specific procedure for creating the correction curves is described below. First, objects with atomic numbers (Z) 3 to 20 were assumed, which have various mass thicknesses ($0.01 \leq \rho t \leq 150$ [g/cm^2]) as shown in Figure A2, and an 18 × 235-pixel image without statistical fluctuation was generated. Then, the corresponding X-ray image (count image) for each energy bin was calculated. The calculations were performed using the X-ray image simulator [36]. The incident polychromatic X-ray spectrum was generated using the semi-experimental formula proposed by Tucker et al. [38]. The leftmost column of the image corresponds to the count of X-rays that did not penetrate the object. Therefore, by using the information in these images, it is possible to calculate $\mu t = \ln\left(\frac{I_0}{I}\right)$ value for all mass thicknesses with different Z materials.

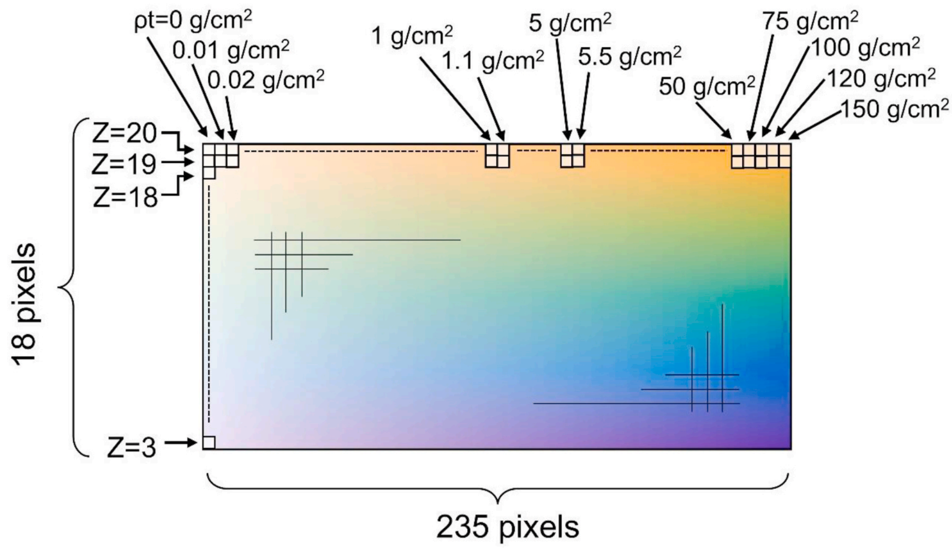

Fig. A2. A design of a phantom image prepared to correct for beam hardening and detector responses. An 18 × 235-pixel image was generated without consideration of statistical fluctuations, and μt values were calculated by analyzing the image.

References

[1] B. Hou, Q. Chen, L. Yi, P. Sellin, H.T. Sun, L.J. Wong, X. Liu, Materials innovation and electrical engineering in X-ray detection, Nat. Rev. Electr. Eng. 1 (2024) 639–655, https://doi.org/10.1038/s44287-024-00086-x.

[2] L. Ren, T. Allmendinger, A. Halaweish, B. Schmidt, T. Flohr, C.H. McCollough, L. Yu, Energy-integrating-detector multi-energy CT: implementation and a phantom study, Med. Phys. 48 (2021) 4857–4871, https://doi.org/10.1002/mp.14943.

[3] R.H.J.A. Slart, M. Punda, D.S. Ali, et al., Updated practice guideline for dual-energy X-ray absorptiometry (DXA), Eur. J. Nucl. Med. Mol. Imag. 52 (2025) 539–563, https://doi.org/10.1007/s00259-024-06912-6.

[4] J.P. Bennett, C.M. Prado, M.C. Gonzalez, S.B. Heymsfield, Clarification and standardization of dual-energy X-ray absorptiometry terminology for accurate scientific communication and clinical diagnostic accuracy, Am. J. Clin. Nutr. 122 (2025) 661–670, https://doi.org/10.1016/j.ajcnut.2025.06.023.

[5] B. Kreisler, Photon counting detectors: concept, technical challenges, and clinical outlook, Eur. J. Radiol. 149 (2022) 110229, https://doi.org/10.1016/j.ejrad.2022.110229.

[6] A. Esquivel, A. Ferrero, A. Mileto, F. Baffour, K. Horst, P.S. Rajiah, A. Inoue, S. Leng, C. McCollough, J.G. Fletcher, Photon-counting detector CT: key points radiologists should know, Korean J. Radiol. 23 (2022) 854–865, https://doi.org/10.3348/kjr.2022.0377.

[7] C.H. McCollough, K. Rajendran, F.I. Baffour, F.E. Diehn, A. Ferrero, K. N. Glazebrook, K.K. Horst, T.F. Johnson, S. Leng, A. Mileto, P.S. Rajiah, B. Schmidt, L. Yu, T.G. Flohr, J.G. Fletcher, Clinical applications of photon counting detector CT, Eur. Radiol. 33 (2023) 5309–5320, https://doi.org/10.1007/s00330-023-09596-y.

[8] C.H. McCollough, K. Rajendran, S. Leng, L. Yu, J.G. Fletcher, K. Stierstorfer, T. G. Flohr, The technical development of photon-counting detector CT, Eur. Radiol. 33 (2023) 5321–5330, https://doi.org/10.1007/s00330-023-09545-9.

[9] J. Greffier, A. Viry, A. Robert, M. Khorsi, S. Si-Mohamed, Photon-counting CT systems: a technical review of current clinical possibilities, Diagn. Interventional Imaging 106 (2025) 53–59, https://doi.org/10.1016/j.diii.2024.09.002.

[10] K. Taguchi, J.S. Iwanczyk, Vision 20/20: single photon counting x-ray detectors in medical imaging, Med. Phys. 40 (2013) 100901, https://doi.org/10.1118/1.4820371.

[11] M. Danielsson, M. Persson, M. Sjölin, Photon-counting x-ray detectors for CT, Phys. Med. Biol. 66 (2023), https://doi.org/10.1088/1361-6560/abc5a5, 03TR01.

[12] K. Taguchi, Energy-sensitive photon counting detector-based X-ray computed tomography, Radiol. Phys. Technol. 10 (2017) 8–22, https://doi.org/10.1007/s12194-017-0390-9.

[13] T. Asahara, S. Okada, H. Hayashi, T. Maeda, R. Nishigami, D. Kobayashi, C. Kurose, N. Kimoto, S. Goto, M. Hisatomi, Y. Yanagi, T. Iguchi, Helpfulness of effective atomic number image in forensic dental identification: photon-counting computed tomography is suitable, Comput. Biol. Med. 184 (2025) 109333, https://doi.org/10.1016/j.compbiomed.2024.109333.

[14] T. Asahara, M. Mitani, N. Kimoto, R. Nishigami, K. Takegami, Y. Morimitsu, N. Akagi, T. Miyoshi, Y. Kanazawa, T. Iguchi, H. Hayashi, Applicability of effective atomic number (Z_{eff}) image analysis of coronary plaques measured with Photon-counting computed tomography, Investig. Radiol. 61 (2026) 378–386, https://doi.org/10.1097/RLI.0000000000001237.

[15] T. Asahara, R. Nishigami, N. Kimoto, M. Mitani, Y. Morimitsu, N. Akagi, F. Higaki, T. Iguchi, T. Hiraki, H. Hayashi, Potential of quantitative X-ray imaging from photon-counting CT: a novel analysis based on effective atomic number and physical density, J. Appl. Clin. Med. Phys. (2026) e70673, https://doi.org/10.1002/acm2.70673.

[16] H. Hayashi, R. Nishigami, T. Asahara, N. Kimoto, D. Kobayashi, M. Mitani, N. Akagi, F. Higaki, T. Iguchi, An algorithm to calculate physical density of biomedical objects having $3 \leq Z_{eff} \leq 20$: an application study using clinical photon-counting computed tomography equipment, Appl. Radiat. Isot. (2026) 112768, https://doi.org/10.1016/j.apradiso.2026.112768.

[17] L.P. Liu, M. Hwang, M. Hung, M.C. Soulen, T.P. Schaer, N. Shapira, P.B. Nöel, Non-invasive mass and temperature quantifications with spectral CT, Sci. Rep. 13 (2023) 6109, https://doi.org/10.1038/s41598-023-33264-2.

[18] P. Trueb, P. Zambon, C. Broennimann, Assessment of the spectral performance of hybrid photon counting x-ray detectors, Med. Phys. 44 (2017) e207–e214, https://doi.org/10.1002/mp.12323.

[19] P. Zambon, V. Radicci, P. Trueb, C. Disch, M. Rissi, T. Sakhelashvili, M. Schneebeli, C. Broennimann, Spectral response characterization of CdTe sensors of different pixel size with the IBEX ASIC, Nucl. Instrum. Methods Phys. Res. Sect. A Accel. Spectrom. Detect. Assoc. Equip. 892 (2018) 106–113, https://doi.org/10.1016/j.nima.2018.03.006.

[20] P. Otfinowski, Spatial resolution and detection efficiency of algorithms for charge sharing compensation in single photon counting hybrid pixel detectors, Nucl. Instrum. Methods Phys. Res. Sect. A Accel. Spectrom. Detect. Assoc. Equip. 882 (2018) 91–95, https://doi.org/10.1016/j.nima.2017.10.092.

[21] D. Pennicard, R. Ballabriga, X. Llopart, M. Campbell, H. Graafsma, Simulations of charge summing and threshold dispersion effects in Medipix3, Nucl. Instrum. Methods Phys. Res. Sect. A Accel. Spectrom. Detect. Assoc. Equip. 636 (2011) 74–81, https://doi.org/10.1016/j.nima.2011.01.124.

[22] K. Taguchi, Multi-energy inter-pixel coincidence counters for charge sharing correction and compensation in photon counting detectors, Med. Phys. 47 (2020) 2085–2098, https://doi.org/10.1002/mp.14047.

[23] D. Bushe, R. Zhang, G.H. Chen, K. Li, Unbiased zero-count correction method in low-dose high-resolution photon counting detector CT, Phys. Med. Biol. 68 (2023) 115002, https://doi.org/10.1088/1361-6560/acd238.

[24] S. Marupudi, J.A. Manus, M.U. Ghani, S.J. Glick, B. Ghammraoui, Evaluation of charge summing correction in CdTe-based photon-counting detectors for breast CT:

performance metrics and image quality, J. Med. Imaging 12 (2025) 013501, https://doi.org/10.1117/1.jmi.12.1.013501.
[25] H. Ding, S. Molloi, Image-based spectral distortion correction for photon-counting x-ray detectors, Med. Phys. 39 (2012) 1864–1876, https://doi.org/10.1118/1.3693056.
[26] N. Kimoto, H. Hayashi, T. Asakawa, C. Lee, T. Asahara, T. Maeda, S. Goto, Y. Kanazawa, A. Katsumata, S. Yamamoto, M. Okada, Effective atomic number image determination with an energy-resolving photon-counting detector using polychromatic X-ray attenuation by correcting for the beam hardening effect and detector response, Appl. Radiat. Isot. 170 (2021) 109617, https://doi.org/10.1016/j.apradiso.2021.109617.
[27] H. Hayashi, N. Kimoto, T. Asahara, T. Asakawa, C. Lee, A. Katsumata, Photon Counting Detectors for X-ray Imaging: Physics and Applications, Chapter 1-5, Springer, 2021, pp. 1–119. ISBN:978-3-030-62679-2.
[28] N. Kimoto, H. Hayashi, C. Lee, T. Maeda, M. Ando, Y. Kanazawa, A. Katsumata, S. Yamamoto, M. Okada, A novel algorithm for extracting soft-tissue and bone images measured using a photon-counting type X-ray imaging detector with the help of effective atomic number analysis, Appl. Radiat. Isot. 176 (2021) 109822, https://doi.org/10.1016/j.apradiso.2021.109822.
[29] R. Nishigami, N. Kimoto, T. Asahara, T. Maeda, D. Kobayashi, S. Goto, T. Haba, Y. Kanazawa, S. Yamamoto, H. Hayashi, Bone-enhanced high contrast X-ray images derived from attenuation estimation related to ultra-low energy X-rays – an application of an energy-resolving photon-counting detector (ERPCD), Radiat. Phys. Chem. 238 (2026) 113243, https://doi.org/10.1016/j.radphyschem.2025.113243.
[30] J.H. Hubbell, S.M. Seltzer, Tables of X-Ray Mass Attenuation Coefficients and Mass Energy-Absorption Coefficients 1 Kev to 20 Mev for Elements Z = 1 to 92 and 48 Additional Substances of Dosimetric Interest, 5632, NIST Publications, 1995.
[31] H. Hirayama, Y. Namito, A.F. Bielajew, J.W. Scott, R.N. Walter, THE EGS5 CODE SYSTEM, SLAC-R-730 and KEK Report 2005−8, Stanford Linear Accelerator Center and High Energy Accelerator Research Organization, 2005. https://rcwww.kek.jp/research/egs/egs5.html.
[32] T. Maeda, H. Hayashi, C. Lee, M. Ando, K. Takegami, N. Kimoto, T. Konishi, S. Murakami, M. Maki, K. Yamashita, K. Higashino, Experimental study of X-ray dose reduction factor when using various size bismuth and lead particles, Radiat. Phys. Chem. 195 (2022) 110049, https://doi.org/10.1016/j.radphyschem.2022.110049.
[33] Acrorad, Home Page of Acrorad Co., Ltd. https://www.acrorad.co.jp/products/technology/basic.html. (Accessed March 2026).
[34] R.B. Firestone, C.M. Baglin, S.Y.F. Chu, Table of Isotopes, eighth ed., 1999. ISBN-13: 978-0471356332.
[35] H. Hayashi, Chapter 4, in: Salim Reza (Ed.), Theoretical Consideration of the Response Function of a Two-Dimensional Cdte Detector, Semiconductor Radiation Detectors, Technology, and Applications, first ed., CRC press, 2017, pp. 85–108. ISBN:9781138710344.
[36] R. Nishigami, D. Kobayashi, N. Kimoto, T. Asahara, T. Maeda, T. Haba, Y. Kanazawa, S. Yamamoto, H. Hayashi, Optimization of energy windows to calculate quantitative X-ray images using an energy-resolving photon-counting detector: a simulation study, Radiat. Phys. Chem. 229 (2025) 112460, https://doi.org/10.1016/j.radphyschem.2024.112460.
[37] J-RIME (Japan Network for Research and Information on Medical Exposure), National Diagnostic Reference Levels in Japan - Japan Drls, 2020. https://j-rime.qst.go.jp/report/DRL2020_Engver.pdf.
[38] D.M. Tucker, G.T. Barnes, D.P. Chakraborty, Semiempirical model for generating tungsten target x-ray spectra, Med. Phys. 18 (1991) 211–218, https://doi.org/10.1118/1.596709.
[39] E. Nazemi, A. Movafeghi, B. Rokrok, M.H. Choopan Dastjerdi, A novel method for predicting pixel value distribution non-uniformity due to heel effect of X-ray tube in industrial digital radiography using artificial neural network, J. Nondestruct. Eval. 38 (2019) 3, https://doi.org/10.1007/s10921-018-0542-9.
[40] N. Kimoto, R. Nishigami, T. Asahara, Y. Kanazawa, A. Katsumata, S. Yamamoto, H. Hayashi, Counting loss correction algorithm for an energy-resolving photon-counting detector for X-ray imaging of biological objects with effective atomic numbers between 3 and 20, Radiat. Phys. Chem. 243 (2026) 113723, https://doi.org/10.1016/j.radphyschem.2026.113723.